22 Jun 2020

One-Dimensional Sensor Learns to Sense Three-Dimensional Space

Chen Zhu

Rex E. Gerald

Yizheng Chen

Jie Huang
Missouri University of Science and Technology, jieh@mst.edu

Recommended Citation

C. Zhu et al., "One-Dimensional Sensor Learns to Sense Three-Dimensional Space," *Optics Express*, vol. 28, no. 13, pp. 19374-19389, Optical Society of America, Jun 2020.
The definitive version is available at https://doi.org/10.1364/OE.395282

Research Article | Vol. 28, No. 13 / 22 June 2020 / Optics Express 19374
Optics EXPRESS

One-dimensional sensor learns to sense three-dimensional space

CHEN ZHU, REX E. GERALD II, YIZHENG CHEN, AND JIE HUANG*

Department of Electrical and Computer Engineering, Missouri University of Science and Technology, Rolla, MO 65409, USA
**jieh@mst.edu*

Abstract: A sensor system with ultra-high sensitivity, high resolution, rapid response time, and a high signal-to-noise ratio can produce raw data that is exceedingly rich in information, including signals that have the appearances of "noise". The "noise" feature directly correlates to measurands in orthogonal dimensions, and are simply manifestations of the off-diagonal elements of 2nd-order tensors that describe the spatial anisotropy of matter in physical structures and spaces. The use of machine learning techniques to extract useful meanings from the rich information afforded by ultra-sensitive one-dimensional sensors may offer the potential for probing mundane events for novel embedded phenomena. Inspired by our very recent invention of ultra-sensitive optical-based inclinometers, this work aims to answer a transformative question for the first time: can a single-dimension point sensor with ultra-high sensitivity, fidelity, and signal-to-noise ratio identify an arbitrary mechanical impact event in three-dimensional space? This work is expected to inspire researchers in the fields of sensing and measurement to promote the development of a new generation of powerful sensors or sensor networks with expanded functionalities and enhanced intelligence, which may provide rich *n*-dimensional information, and subsequently, data-driven insights into significant problems.

1. Introduction

Fiber-optic sensors (FOSs) have been successfully used in an expansive range of sensing applications, such as structural health monitoring, down-hole monitoring, chemical and biological sensing, and seismic detection, over the past four decades [1–5]. The tremendous growth of FOSs in engineering societies is mainly owing to the fact that FOSs outperform traditional electronic sensors and provide unique advantages, including their diminutive size, high sensitivity and resolution, immunity to electromagnetic interference, remote operation, and broad capabilities for multiplexing and distributed sensing [1].

In the past decade, the emergence of various high-quality, high-speed, high-fidelity, miniaturized, and affordable optoelectronic components and devices has contributed to the advancements in FOSs with improved functionality. A series of novel FOSs that provide unprecedented performance (such as ultra-high sensitivity and resolution, as well as ultra-fast update rates) have been developed [6–11]. For example, Gagliardi *et al.,* demonstrated strain measurements at the 10^{-13} ε/Hz$^{1/2}$ level using a fiber Bragg grating (FBG) resonator with a diode laser source that was stabilized against a quartz-disciplined optical frequency comb [6]. Miniaturized manometers with sub-Pascal resolution [7] and microphones/hydrophones with a minimum detectable pressure as low as approximately 1 μPa/Hz$^{1/2}$ [8,9] have also been made possible. Ultrasensitive optical fiber-tip microresonators were demonstrated for photoacoustic and ultrasound imaging, with broadband acoustic responses up to 40 MHz and noise-equivalent pressures as low as 1.6 mPa/Hz$^{1/2}$ [10]. FBG interrogation techniques with ultra-fast sampling speed up to MHz levels have been reported [11], opening new avenues for FBG sensing in various applications such as blast tests, ultrasonic nondestructive tests, and engine diagnostic tests. Such advanced sensing

#395282 https://doi.org/10.1364/OE.395282
Journal © 2020 Received 16 Apr 2020; revised 30 May 2020; accepted 5 Jun 2020; published 16 Jun 2020

Optics EXPRESS

techniques provide complex and rich information from measurements, including the expected signals and abnormal "noise", which has conventionally been undetectable and uninterpretable. Therefore, a challenge that is currently faced by researchers in the sensing field is how to extract as much useful information as possible from the data obtained from FOSs, and how to gain new insights from the prodigious information, which may lead to new discoveries in fundamental physics and applications in the engineering sciences. Machine learning (ML) may play a significant role in addressing this challenge.

ML techniques have enabled substantial breakthroughs in the traditional computer science fields in the past decade (e.g., machine vision and natural language processing) [12]. Researchers from other areas have also started to adopt these data-driven techniques, thereby extending the scope of ML applications to enable new discoveries more broadly. Promising achievements have been made in several fields, such as the solid earth geosciences [13,14], remote sensing [15,16], seismology [17,18], and clinical and medical research [19,20].

Pioneering research has already begun to explore the potential of combining ML with state-of-the-art fiber-optic sensing and communication techniques. Artificial neural networks (ANNs) have been used to recognize and reconstruct images, distorted by the multimodal interferences obtained from multimode fibers, by analyzing complex speckle patterns [21–24]. A preliminary study aimed at turning the optical fiber specklegram sensor into a spatially resolved sensing system was also conducted based on the assistance of ML (ANNs) [25]. Several studies have demonstrated the capabilities of rapidly interrogated FBGs for the identification of damaged zones near the perimeter of sensors enabled by ANNs (e.g., within a radius of 0.5 m) [26,27]. A real-time event classification system based on fiber-optic perimeter intrusion detection techniques (i.e., distributed FOSs) and ANNs was presented for classifying numerous intrusion and non-intrusion events [28].

In this study, we present a novel application of ML in the field of sensing and instrumentation. A high-resolution one-dimensional (1-D) fiber-optic inclinometer (FOI) system was "trained" and "learned" to recognize the positions of the sources of vibrations induced by single blunt-force impact events in the three-dimensional (3-D) space surrounding the FOI. We postulate that the anisotropy of the 3-D space surrounding the FOI makes it possible for a 1-D sensor to sense 3-D space. That is, the fundamental physics describing the transient mechanical forces along a single spatial coordinate at a point in space in response to an arbitrary impulse force in that same space is predicated on the anisotropic distribution of matter in the macro-space and anisotropic structures in the micro-space surrounding the FOI. Thus, the spatial anisotropy of matter, viewed from the FOI position, makes it possible to map arbitrary impulse forces in the surrounding 3-D space to the single coordinate measured by the FOI. Complicated mappings can be learned by employing ML methods. Hence, we used the FOI system to collect a large number of responses to vibrations, each caused by a single blunt-force impact event to the substrate on which the FOI was mounted. These FOI responses were used to train, validate, and test various ML algorithms. In this study, we did not attempt to provide a comprehensive and detailed analysis of the manners in which the vibrations, induced by specific mechanical impact events, were propagated to the FOI. Instead, our aim was to provide a proof of concept that demonstrates the capabilities of the ML-assisted 1-D FOI as a smart sensor system for identifying spatially resolved mechanical impact events in 3-D space (e.g., determining the position and magnitude of an impulse force on a substrate that is coupled to the FOI).

2. Methods

2.1. FOI system

We firstly introduce a high-resolution FOI, with high sensitivity owing to a low-inertia mechanical structure. Schematics illustrating the essential elements and operation of the internal structure of the 1-D FOI, along with a photograph of a prototype inclinometer, are presented in Fig. 1.

Optics EXPRESS

Figure 1(a) shows a schematic of the side view of the FOI. The FOI consists of two parts: the mass block part serving as the element that is responsive to tilt, and the optical fiber module serving as a Fabry–Pérot cavity for measuring the tilt. The mass block is connected to the top frame of the FOI by two flexible stainless steel multi-strand ropes. The two ropes have the same length l, and the four connection points, as depicted by the circles in Fig. 1(a), are contained in a common plane. Therefore, a parallelogram is formed among the mass block, top frame, and two ropes, with the four connection points as the four vertices. A layer of gold is coated onto the endface of the mass block and serves as a mirror. A section of optical fiber held by a ceramic ferrule is connected to the top frame of the FOI by means of a rigid supporting rod. The supporting rod is fixed perpendicularly to the top frame so that the optical fiber endface is parallel to the mirror on the mass block. Consequently, a Fabry–Pérot cavity is formed between the optical fiber endface and external mirror, with a length of d (the distance between the optical fiber endface and mirror). When the FOI is titled to an angle θ, the length of the cavity, which constitutes the fundamental parameter of a Fabry–Pérot interferometer (FPI), will change, as illustrated in Fig. 1(b). The process can be described as follows: as the FOI is tilted, the optical fiber module will also be inclined to the same angle owing to the rigid connection. However, the two ropes used to connect the mass block will remain perpendicular to the horizontal plane, prescribed by the direction of the gravity force. Owing to the constraints of the parallelogram geometry, the mirror and optical fiber endface remain parallel; thus, the FPI configuration still holds. The principal concept of the FOI is to use the FPI to measure the displacement of the mass block when it is subjected to tilt and thereby measure the tilt angle. According to the geometric relationships, the change in the applied tilt angle ($\Delta\theta$) leads to a change in the measured cavity length of the FPI (Δd):

$$\Delta\theta = \arcsin\frac{\Delta d}{l}, \tag{1}$$

where l denotes the length of the ropes. Equation (1) can be simplified to $\Delta\theta \approx \Delta d/l$ when the change in the tilt angle is very small. The measurement resolution of the FOI is determined by the rope lengths: greater lengths result in higher resolution. Detailed studies of the FOI can be found in our recent work [29].

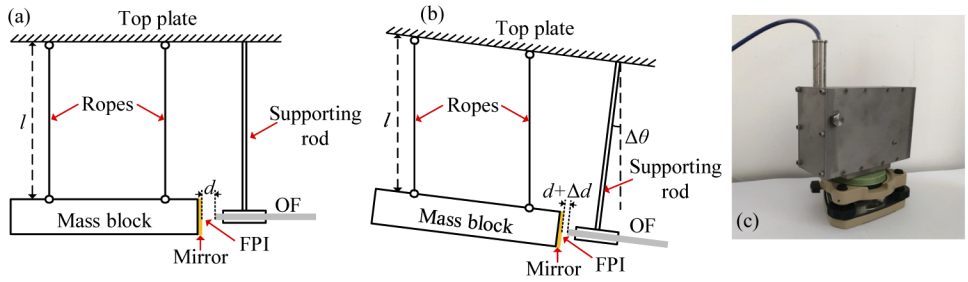

Fig. 1. Schematics of FOI demonstrating 1-D tilt function, and a photograph of a prototype device [29]. (a) Schematic of a side view of the FOI at a tilt angle of zero degrees. OF: optical fiber. (b) Schematic of the FOI tilted to angle $\Delta\theta$. (c) Photograph of a prototype FOI packaged in a box made of Invar alloy, which has a low coefficient of thermal expansion. The combination of Invar alloy and judicious system designs can reduce the temperature effects on the FOI, resulting in more accurate tilt measurements. The 1-D inclinometer was mounted on a total station tribrach, through which the initial tilt angle of the FOI could be flexibly adjusted.

A photograph of a prototype FOI device is presented in Fig. 1(c), where the sensor structure illustrated in Fig. 1(a) was packaged in a box made of Invar alloy. The rope lengths were designed as 6.0 cm. The theoretical measurement resolution of the FOI was determined to

Optics EXPRESS

be approximately 17 nanoradians, provided that the change in the cavity length (Δd) could be resolved to 1 nm [29,30]. The prototype FOI was mounted on a total station tribrach, as illustrated in Fig. 1(c). By adjusting the three tribrach supports, the initial tilt angle applied to the FOI can be adjusted arbitrarily. We postulated that the base substrate on which the FOI was mounted acted as an anisotropic mechanical transducer. Thus, in the most general case, the nine elements of a non-symmetric second-rank tensor at the position of the FOI described the transient force along the FOI 1-D sensing coordinate caused by an arbitrary impulse force in the surrounding 3-D space. Consequently, in principle, the 1-D FOI was able to unambiguously identify the source of the vibrations located at an arbitrary position in the 3-D space surrounding the FOI.

A schematic of the FOI system that included an interrogation module is presented in Fig. 2. An amplified spontaneous emission (ASE) light source with a wavelength output range of 1.53 to 1.61 μm (ASE-FL7002-C4) was used to illuminate the Fabry–Pérot cavity of the FOI sensor. The illumination light was launched into the FOI sensor via a broadband single-mode fiber-optic circulator. After that, the reflected light from the FOI sensor was directed to the light detector by the circulator. The light detector employed in the system was a near-infrared spectrometer (FGBA interrogation analyzer, BaySpec) with 512 pixels for each spectrum and a fast frequency response of up to 5 kHz. The spectra acquired by the spectrometer were synchronously streamed to a PC and processed using a high-speed demodulation algorithm.

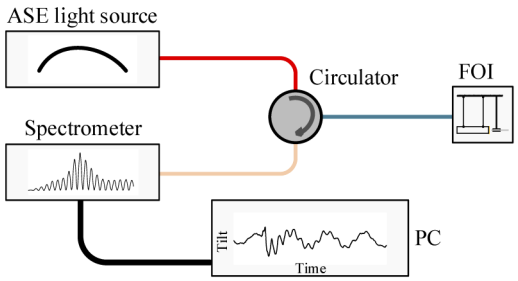

Fig. 2. Schematic of FOI system, including FOI sensor and interrogation module. A high-speed spectrometer was employed in the system, which has a fast frequency response of up to 5 kHz. The ASE light source was used as the broadband laser source to illuminate the Fabry–Pérot cavity. A spectrometer was employed to collect the reflected light from the Fabry–Pérot cavity. The acquired data were synchronously streamed to the PC and processed by a high-speed demodulation algorithm, illustrating the instantaneous change in the cavity length (i.e., the tilt angle) experienced by the FOI as a function of time.

2.2. *Impact events in surrounding space*

Two sets of experiments were designed to validate our expectation that the ML-assisted FOI system could identify the positions of the vibration sources in the surrounding space, as illustrated in Fig. 3. The first experiment was designed to demonstrate that the system could distinguish among eight different positions on a ground floor supporting the FOI, i.e., a two-dimensional (2-D) plane. In contrast, the second experiment was performed to demonstrate that the system could distinguish among 14 different positions in the 3-D space surrounding the FOI. By generating a large number of vibrations from the same positions in the surrounding space of the FOI, recording the transient responses of the FOI, processing them, and training these processed datasets with ML algorithms, it was possible to predict the positions where new impact events occurred in the 3-D surrounding space.

Optics EXPRESS

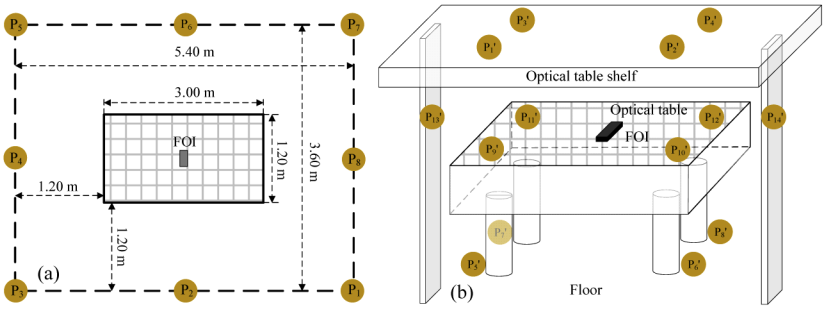

Fig. 3. Schematics of experiments designed to demonstrate the capability of the ML-assisted FOI system for predicting the positions of blunt-force impact events occurring in space surrounding the FOI system. (a) Illustration of a top view of the first experiment designed to demonstrate the capability of the ML-assisted FOI system for predicting the positions of impact events occurring on a 2-D ground substrate. The FOI sensor was placed at the center of an optical table that was on the floor (substrate). The height of the optical table was 0.92 m. Eight different positions surrounding the optical table were selected for the experiment. Vibrations were produced at these eight floor positions by human step-on-floor actions. (b) Schematic of a side view for the second experiment, designed to demonstrate the capability of the ML-assisted FOI system for predicting positions of impact events in the surrounding 3-D space. The heights of the optical table and optical table shelf from the floor were 0.92 m and 1.71 m, respectively. The size of the tabletop of the optical table was 3.00 × 1.20 m; the size of the optical table shelf was 3.06 × 0.66 m. A total of 14 different positions in the surrounding 3-D space were selected for the sensing experiment. Vibrations were produced at these 14 positions by hammer-hitting actions. The vibrations caused by the blunt-force impact events at positions other than P_9' to P_{12}' were transmitted to the floor and subsequently to the optical table. The tilt angles experienced by the optical table owing to the blunt-force impact events were measured by the high-resolution FOI. The transient responses of the FOI following processing were used to train, validate, and test the ML algorithms.

2.2.1. Impact events on 2-D ground floor

For the first experiment, which was designed to demonstrate the capability of the ML-assisted FOI system for predicting the vibration sources on a 2-D ground plane, the FOI was placed at the center of an optical table, as schematically indicated in Fig. 3(a). The optical table was supported by the floor. A volunteer stepped onto the floor surrounding the optical table to apply blunt-force impacts to the floor. The blunt-force impacts caused vibrations in the floor that were transmitted to the optical table, and subsequently to the FOI sensor. The transient responses of the FOI sensor to the blunt-force impacts were recorded by the interrogation module. Eight different labeled positions were tested to verify the capability of the FOI for discriminating the positions of the blunt-force impact events, as indicated in Fig. 3(a). At each position, 62 individual impact events were simulated, with a time interval of 4.0 s between events. The interrogation system was operated continuously during the experiments. The time transient signal, within a period of 4.0 s for each impact event, was subsequently extracted and adequately labeled for later data processing. A total of 5000 spectra (where each spectrum consisted of 512 pixels) were recorded each second. Approximately ten million spectra were recorded during the experiments. Prior to performing the position-of-impact-event classification experiment, the capability of the FOI for quantifying the magnitude of the impact was investigated. Specifically, different magnitudes of the impact were caused by a plastic bottle that contained 1 L of water falling from different heights from the ground. As the bottle hit the ground, vibrations were generated in the floor and transmitted to the optical table, where they were measured by the high-resolution FOI sensor.

Optics EXPRESS

Different impact magnitudes corresponding to the different tilt angles measured by the FOI were expected. The impact magnitude quantification experiments were performed at position P_2, as indicated in Fig. 3(a).

2.2.2. Impact events in 3-D space

The layout of the second experiment, which was designed to demonstrate the capability of the ML-assisted FOI system for discerning the position of a blunt-force impact event in 3-D space, is schematically presented in Fig. 3(b). A total of 14 different positions in the 3-D space in which the FOI was placed were selected for the demonstration. The 14 selected positions are designated with the labels P_1', P_2',. . . , and P_{14}' in Fig. 3(b), and included four positions on the top of the optical table shelf, four positions on the ground floor, four positions on the optical table, and two positions on the side frames of the optical table shelf system. Similar experiments to those discussed in Section 2.2.1 were performed. At each position, 62 individual impact events were created, with a time interval of 4.0 s between events. Instead of using human step-on-floor actions, a hammer was used as the impacting implement. Numerous time responses of the FOI system to these impact events were recorded. These datasets were processed and subsequently used to train, validate, and test the ML algorithms.

2.3. Data processing

During the process of recording a spectrum in the experiment, the real-time spectrum from the FOI sensor was processed and the corresponding cavity length was extracted. Different data folders (8 folders for the first experiment and 14 for the second experiment) containing the cavity length information, corresponding to the different positions where the vibrations were caused, were created. Each data folder included 62 datasets, corresponding to the 62 individual impact events. In the preliminary test, we observed that the effect of the vibration on the FOI was diminished within approximately 2.0 s. Therefore, for each dataset (i.e., an individual blunt-force impact event), the recorded dominant response of the FOI sensor in a time period of 2.0 s was extracted. The transient responses of the FOI to the impact event were included in the 2.0 s time period. All the datasets (a total of 496 and 868, i.e., 62×8 and 62×14; each dataset consisted of 10,000 cavity length determinations in a time period of 2.0 s) were converted into tilt angles based on the FOI calibration curve. The tilt angle datasets were subsequently used for further processing (i.e., feature extraction).

Prior to training the ML algorithms, a wavelet time-scattering transform was applied to each dataset to extract the frequency features representing the transient oscillatory motions experienced and measured by the FOI. The wavelet transform, similar to the Fourier transform, is a type of transform that provides the time-frequency representation of a signal. The multi-resolution feature of the wavelet transform avoids the deformation instabilities of the Fourier transform from the time domain to the frequency domain owing to Heisenberg's Uncertainty Principle [31]. By combining wavelet transforms with scattering frameworks, a wavelet time-scattering framework was demonstrated as an effective tool to derive, with minimal configuration, low-variance features from various time series (e.g., human electrocardiogram signals and phonocardiogram recordings) for classification and regression in ML applications [32,33]. In this case, a wavelet time-scattering framework including two wavelet filter banks with quality factors of 8 and 1, and an invariance scale of 1, was used. The mean scattering features for each dataset were obtained following the transformation, and these features (271 for each dataset; a total of 496×271 and 868×271) were input into the ML algorithms to train, validate, and test the models.

Two different ML algorithms were employed in the test, i.e., the support vector machine (SVM) and the ANN. The SVM was originally designed for binary classification by identifying the optimal boundary that separates the training data into two different classes [34]. The data points that are closest to the separating boundary are known as support vectors. The SVM model

Optics EXPRESS

uses kernel functions (linear and nonlinear) to map the training data into a higher-dimensional feature space. For example, a linear kernel model separates two classes using a hyperplane, while nonlinear kernel models (such as Gaussian, cubic, and quadratic functions) allow for nonlinear decision boundaries between the two classes. The SVM binary model can be extended into a multiclass classifier by fusing several of its kind using different frameworks, such as error-correcting output codes (ECOC) [35,36]. Linear kernel SVMs combined with ECOC were employed in the demonstration. During the model training, a 10-fold cross-validation scheme was used as the method for assessing the preliminary predictive accuracy of the model. The other ML algorithm used in the test was the ANN. ANNs are among the dominant algorithms in the ML field [37–39]. ANN models were initially inspired by the interconnected networks of biological neurons in the human brain; therefore, ANNs learn from training data in a manner that mimics the human learning processes [40]. ANNs are constructed with connections of nodes (neurons) associated with a set of weight values. Each node takes a weighted sum of values from the previous layer and yields an output that is passed to the subsequent layer via an activation function. In a back-propagation neural network, the weight values connected to each node are optimized using back-propagation algorithms to obtain minimal errors between the ANN outputs and targets. A shallow ANN (with a single hidden layer) was constructed and trained in our case for the datasets obtained from the first experiment, as schematically presented in Fig. 4. The shallow ANN included an input layer with 271 nodes corresponding to the 271 features of each dataset, a hidden layer with ten nodes, and an output layer with eight nodes corresponding to the eight different classes (i.e., the eight different positions of the vibration source). The transfer functions for the hidden layer and output layer were a tangent sigmoid function and a softmax function, respectively [41]. The ANN was trained with the scaled conjugate gradient method using the cross-entropy-driven back-propagation algorithm. In the training step, the collected datasets were randomly divided into 70% training, 15% validation, and 15% testing sets.

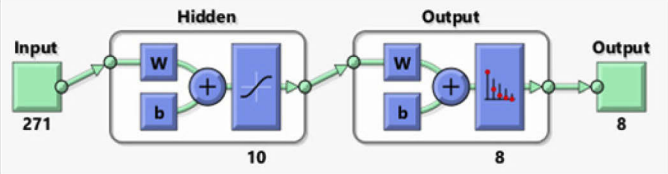

Fig. 4. The topological structure of shallow ANN developed for the first experiment, designed to demonstrate the capability of an ML-assisted FOI system for predicting vibration sources from eight different positions on the 2-D ground floor. The ANN included an input layer with 271 nodes, a single hidden layer with ten nodes, and an output layer with eight nodes. The labels w and b represent the weights and biases in the network, respectively. For the network training, the 496 collected datasets were randomly divided into 70% training, 15% validation, and 15% testing sets.

3. Results

3.1. FOI calibration

The capability of the FOI for probing the changes in the tilt angles was first demonstrated, and the results are presented in Fig. 5. Figure 5(a) provides an example of the recorded interference spectrum from the FOI, recorded by the high-speed spectrometer. A series of peaks and dips can be observed in the spectrum, which resulted from the interference of two reflected light beams in the FOI (Fabry–Pérot interference). By analyzing the interference pattern, the cavity length of the FOI at the original tilt setting was determined to be 345.625 μm. The responses of the FOI to the applied changes in the tilt angles are illustrated in Fig. 5(b). In the calibration experiment, a

Optics EXPRESS

commercial tiltmeter with a measurement accuracy of ±15 μrad was employed as the calibration reference. A tilt angle range of 0 to 8.720 mrad was applied to the FOI in increments of 0.872 mrad. A linear curve fit was applied to the measured dataset, and as expected, an excellent linear relationship was obtained. According to the calibration result, the rope lengths were calculated to be 6.004 cm (see Eq. (1)), which matched well with the sensor design. Note that, in the calibration experiment, an oscillation dampening device was used in the FOI to resist the natural oscillations of the pendulum (the natural oscillations and vibrations derived from the environment) [29]. For the later experiments in which the FOI was used for measuring impact events, the dampening device was removed so that the FOI could capture the instantaneous changes in the tilt angles induced by the surrounding vibrations.

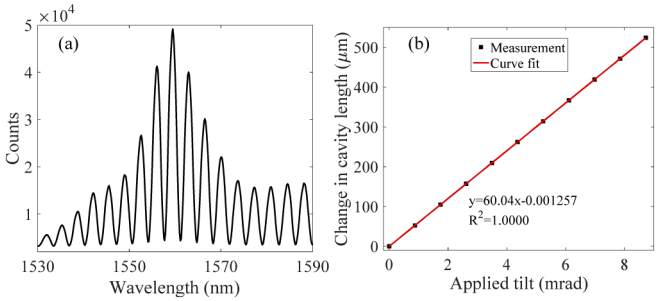

Fig. 5. Demonstration of the FOI capability for probing changes in tilt angles. (a) Example of the reflection spectrum of FOI recorded by the high-speed spectrometer. (b) The response of the FOI to changes in tilt angles for the range 0 to 8.720 mrad, depicted by black dots. A linear curve fit was applied to the dataset, depicted by the solid red line.

3.2. Quantification of blunt-force impact events

The capability of the FOI for quantifying the magnitudes of the blunt-force impact events in the space surrounding the FOI was also demonstrated, as illustrated in Fig. 6. A plastic bottle containing 1 L of water was dropped from four different heights (0.30, 0.63, 0.94, and 1.25 m) onto the floor at a lateral distance of 1.80 m from the FOI to simulate different magnitudes of blunt-force impact events on the floor, corresponding to different potential energies of approximately 2.94, 6.17, 9.21, and 12.25 J, respectively. The responses of the FOI system to these blunt-force impact events are presented in Fig. 6(a). Transient responses of a similar form were obtained for the different blunt-force impact events of varying magnitudes, exhibiting an instant increase in the measured tilt angle of approximately 30 μrad for the largest blunt-force impact event, and diminishing for the other events. Note that the blunt-force impact event-induced changes in the tilt angles recorded by the FOI were relatively small (μrad scale), and below the detection limit of the majority of reported FOIs. The natural low-frequency oscillation of the undamped pendulum was also observed, after the initial blunt-force impact event-induced high-frequency effect on the pendulum diminished. The most evident difference in the series of responses was the peak magnitude of the time transient of the change in the measured FOI tilt angle. The first maximum in the time transient of the change in the tilt angle owing to the blunt-force impact event on the floor measured by the FOI as a function of the potential energy of the water bottle is plotted in Fig. 6(b). Higher potential energies resulted in larger peak changes in the tilt angles that were measured in the potential energy series by the FOI. Therefore, the FOI could quantify the magnitudes of the blunt-force impact events that occurred at one position in the surrounding space of the FOI.

Optics EXPRESS

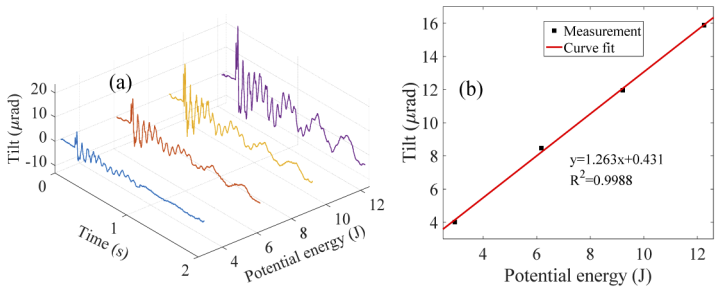

Fig. 6. The capability of the FOI for quantifying magnitudes of blunt-force impact events caused by a 1 L water bottle dropped onto the floor 1.80 m laterally away from the FOI. The FOI was positioned at the center of an optical table, 0.92 m above the floor. (a) Recorded temporal transient responses from the FOI following blunt-force impact events for time periods of 2.0 s. Four blunt-force impact events with different potential energy magnitudes were created at P_2 (see Fig. 3(a)). Transient responses of a similar form were obtained from the FOI. The peak magnitudes of the measured changes in the tilt angles exhibited apparent differences. (b) The first maximum from each one of the tilt angles versus time transients measured by the FOI plotted as a function of the corresponding potential energies of the blunt-force impact events, depicted by black dots. A linear curve fit was applied to the dataset, depicted by the solid red line. The potential energy was defined by the product of the gravitational force exerted by the bottle (i.e., 1 kg × 9.8 m/s^2) and the height from which it was dropped.

3.3. Positions of vibration sources on 2-D ground floor

In the first experiment, the vibrations were caused by blunt-force impact events at eight different positions on the ground floor. Figure 7 presents examples of the time-domain dynamic responses of the FOI, following the initial impacts, for a period of 2.0 s (i.e., the measured changes in the tilt angles versus time) to the vibrations created at the eight different positions surrounding the FOI, illustrated in Fig. 3(a). The measured changes in the tilt angles by the FOI were within the range of several μrad. Differences could be observed between the eight different transient oscillatory signals, but it was challenging to unambiguously correlate the time-domain signals to the eight distinct causes of vibrations by direct visual inspections. We employed the wavelet time-scattering transform to extract the frequency-domain features of these non-stationary signals. The mean scattering features, totaling 271 for each transient vibration event (a total of 496 events) were subsequently obtained from the scattering feature matrix for the scattering decomposition framework and input time-domain signals. These mean scattering features (represented by a 496 × 271 matrix) were used as the input for training the ML algorithms.

The ML training processes were implemented using MATLAB 2018b, installed on a PC with 8 GB of RAM and running Windows 10. The typical computation time for running an ML algorithm on the largest datasets was less than 1 min. Figure 8 presents the training results (categorizations) of the input datasets using a linear SVM model in the form of a confusion matrix [25]. The confusion matrix represents the number of input datasets that the algorithm categorized. For example, for vibrations created at P_1, i.e., the first row, 60 out of 62 datasets were correctly classified into P_1; 2 datasets were categorized into P_4; and, the model successfully classified vibrations created at P_1 from the 8 different vibration sources with an accuracy of 96.8%. Average prediction accuracy of approximately 99% was obtained for the task of identifying the eight classes (eight different vibration sources) using the linear SVM model. Table 1 displays the prediction accuracies achieved when using the SVM models with different kernel functions (including quadratic, cubic, and Gaussian) and other commonly used classifiers, i.e., the fine tree, linear discriminant (LD), and k-nearest neighbor (KNN). It is clear that the linear SVM model

Optics EXPRESS

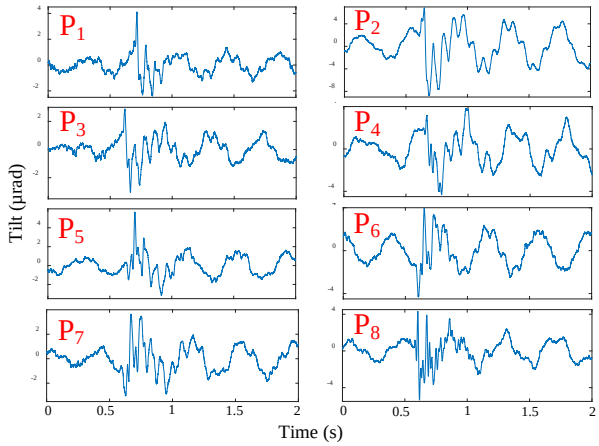

Fig. 7. Examples of time-domain dynamic responses of the FOI to vibrations caused by blunt-force impact events at eight different positions on the ground floor illustrated in Fig. 3(a). The vibrations were caused by human step-on-floor actions. Each blunt-force impact event occurred at the time point of approximately 0.6 s in the transient plots. The measured changes in the tilt angles by the FOI were in the range of several μrad.

provided the highest prediction accuracy, while the more sophisticated Gaussian SVM exhibited the worst performance, with an accuracy of only 53%.

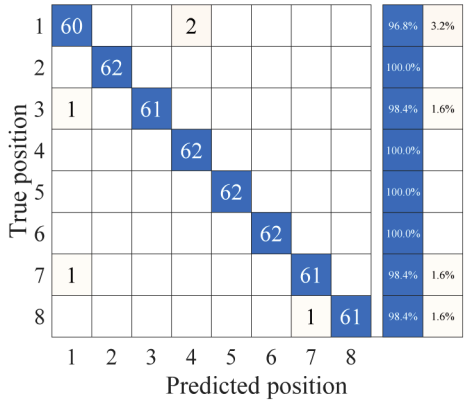

Fig. 8. Confusion matrix of classification of input datasets using a linear SVM model for predicting positions of vibration sources on the 2-D ground floor. At each position, 62 individual blunt-force impact events were created, and the corresponding responses were recorded. The confusion matrix displays the identification accuracy for each class, i.e., each position of the vibration source, using the linear SVM classifier.

Table 1. Prediction accuracies using various ML classifiers [a]

	Linear SVM	Quadratic SVM	Cubic SVM	Gaussian SVM	Fine Tree	LD	KNN
Accuracy (%)	98.8	97.8	97.4	53.2	83.9	67.8	87.7

[a]Results obtained from the investigations that employed various ML classifiers to predict positions of vibration sources on the 2-D ground floor.

Optics EXPRESS

In addition to the SVM models, a shallow ANN was also developed and trained in the experiment. Figure 9 presents the training results of the ANN model. Figure 9(a) plots the cross-entropy error as a function of the epochs in the training process [42]. The cross-entropy error decreased as the training epoch increased, indicating that the prediction accuracy of the ANN model continued to increase as the training epoch increased. The network training was terminated when the generalization ceased to improve, to prevent overfitting, as indicated by the green circle in Fig. 9(a). At this point, the best validation performance for the ANN model (with the minimal cross-entropy error) was obtained. Figure 9(b) illustrates the classifications achieved using the model after 56 epochs of training (at the epoch marked by the green circle in Fig. 9(a)). A categorization accuracy of 100% was obtained, indicating that the ANN model functioned extremely effectively for this multi-class categorization task; that is, it could identify the vibration sources from the eight possible positions. We retrained the model 10 times, and high accuracies were similarly obtained: 99.6%, 100%, 99.2%, 98.6%, 99.8%, 99.8%, 99.8%, 100%, 99.8%, and 100%. The shallow ANN was also trained with different functions such as Levenberg–Marquardt and gradient descent with momentum, with which accuracies greater than 99% were also obtained.

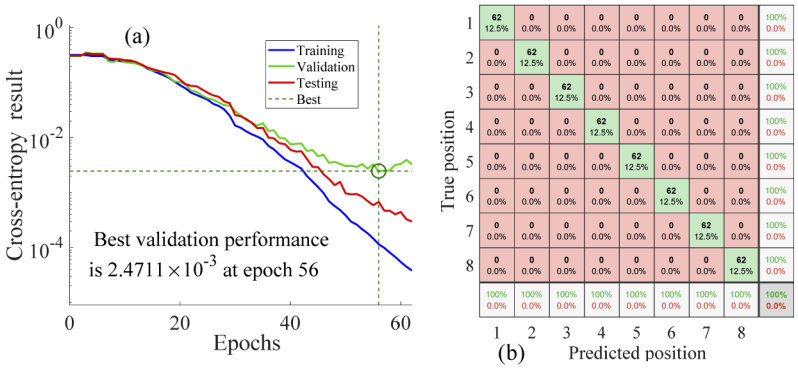

Fig. 9. Results from investigations obtained when using shallow ANN to predict positions of vibration sources on the 2-D ground floor supporting the FOI. (a) Cross-entropy error as a function of epochs in the training process. The cross-entropy error for the training sets decreased as the training epochs increased. Similar decreases in the cross-entropy error were also obtained in the validation and testing sets, indicating that the network could generalize and fit effectively. The network training ended when the generalization ceased to improve, to prevent overfitting, as indicated by the green circle, where the best validation performance for the ANN model (with the minimal cross-entropy error) was obtained. (b) Confusion matrix of the classification results using ANN, indicating the identification accuracy for each class, i.e., each position of the vibration source. At each position, 62 individual datasets were recorded and used in the ML training experiments. Within the experimental uncertainties, a 100% identification accuracy was achieved in the training result.

3.4. *Positions of vibration sources in 3-D space*

Based on the surprisingly-good results obtained in the first experiment, in which vibrations were caused on the 2-D ground floor, we decided to increase the system complexity by expanding the vibration sources to positions in 3-D space. A hammer was employed as the impacting implement, and the vibrations caused by blunt-force impact events at 14 different positions, as indicated in Fig. 3(b), were examined. Figure 10(a) shows examples of time-domain dynamic responses of the FOI to vibrations caused by blunt-force impact events at the 14 different positions. The mean scattering features (an 868 × 271 matrix) obtained from the wavelet time-scattering transform

Optics EXPRESS

were used as the input for training the two ML algorithms (SVM and ANN). An average accuracy of greater than 99% was obtained when using the linear SVM model. The confusion matrix obtained using a shallow ANN for training the datasets is presented in Fig. 10(b). Once again, high prediction accuracy of greater than 99% was obtained when using the ANN model. Only one dataset out of 896 datasets (in the third row of the confusion matrix) was misclassified in the experiment. The ANN model used in this case was the same as the ANN model used in the first experiment (see Fig. 4), except that the number of nodes for the output layer was adjusted to 14, corresponding to the 14 different positions of the blunt-force impact events.

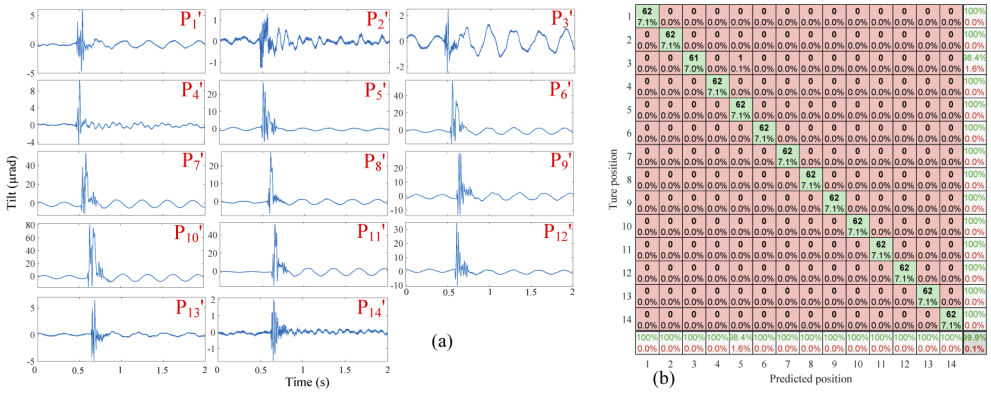

Fig. 10. Results from investigation of impact events in the 3-D space surrounding the FOI. (a) Examples of time-domain dynamic responses of the FOI to vibrations caused by blunt-force impact events at 14 different positions in 3D space surrounding the FOI illustrated in Fig. 3(b). The vibrations were caused by hammer-hitting actions. Each blunt-force impact event occurred at a time point of approximately 0.6 s in the transient plots. The measured changes in the tilt angles by the FOI were within the range of tens of μrad. (b) Results obtained when using the ANN model to predict positions of vibration sources in the 3-D space surrounding the FOI. The ML classification results are presented in the form of a confusion matrix, which indicates the prediction accuracy for each class, i.e., each position of the vibration source in the 3-D space surrounding the FOI. At each position, 62 datasets were used (corresponding to 62 individual blunt-force impact events), and a total of 896 datasets were obtained for the training process. Only one dataset out of 896 datasets (in the third row of the confusion matrix) was misclassified in the experiment. Note that the shallow ANN model was the same as the model used in the first experiment, except that the output layer had 14 nodes. The 14 nodes corresponded to the 14 different positions of the vibration source in the 3-D space.

4. Discussion

A system composed of a single high-resolution 1-D FOI, combined with several ML algorithms, was demonstrated to localize the source of vibrations at positions in the surrounding space of the FOI efficiently and accurately. The accuracies for the 8-class/14-class identification task (8/14 different positions of the vibration sources) were excellent when using two simple yet powerful ML models, i.e., SVM (approximately 99%) and shallow ANN (approximately 100%). The first key element of this work was the high-resolution FOI, which combined a two-rope suspended pendulum structure and a high-resolution optical fiber interferometer. When an impact occurred on the floor in the surrounding space of the FOI, the FOI experienced changes in tilt angles within a range of several μrad owing to the subtle distortions of the ground substrate. The displacements of the pendulum as a result of the transient changes in the tilt angles were measured by an optical fiber FPI, which was formed between the optical fiber endface and a mirror on the pendulum,

Optics EXPRESS

with sub-nanometer displacement resolution. The blunt-force impact event-induced vibrations, which originated from the surrounding space of the FOI, caused changes in the tilt angles of the substrate that supported the FOI, and the changes in the tilt angles were measured by the FOI system. The oscillatory transient signals measured by the FOI system could be considered as "fingerprints" corresponding to unique blunt-force impact events in the 3-D space surrounding the FOI. We postulated that the base substrate on which the FOI was mounted acted as an anisotropic mechanical transducer, whereby a non-symmetric second-rank tensor at the FOI position described the transient force measured by the 1-D FOI system along one coordinate caused by an arbitrary impulse force in the same 3-D space. Additionally, a tiny torque along the coordinate in the FOI could also contribute to the total transient force measured by the 1-D FOI system. As a result, in principle, the 1-D FOI could unambiguously identify the positions of the source of vibrations caused by blunt-force impact events on the ground plane.

In a proof of concept, the vibrations caused by blunt-force impact events (human step-on-floor actions and hammer-hitting actions) at various positions in the surrounding space of the FOI were investigated. The corresponding transient responses of the FOI to these vibrations were recorded. A wavelet time-scattering framework was employed to preprocess the time-domain transient responses of the FOI, in which the frequency-domain features, namely the fingerprints corresponding to each position of a blunt-force impact event, were obtained. Subsequently, the second key element, i.e., the ML models, learned from these features and outputted accurate identifications of the test events, i.e., accurate classifications of the responses of the FOI to different positions of a set of blunt-force impact events. The capability of the ML-assisted FOI system for predicting the positions of the source of the vibrations created on the 2-D ground floor physically supporting the FOI was initially demonstrated. In the second experiment, the vibrations were created in a more complicated environment, i.e., the 3-D surrounding space of the FOI. The ML-assisted FOI system once again exhibited satisfactory performance, with a prediction accuracy greater than 99%. Note that, during the data collection process, the vibrations were caused by human step-on-floor or hammer-hitting actions, which were not exactly reproduced, especially the magnitude. Therefore, different degrees of variation were essentially embedded in the recorded datasets. However, the ML models still yielded highly satisfactory performances. It is noteworthy to mention that the ML tool must be retrained if the position of the FOI in the 3-D space is changed.

The novel technique of combining a high-resolution FOI system and ML methods can locate the positions of a source that causes vibrations in the 3-D space surrounding the FOI by analyzing the transient data signals from the FOI system. The positions of the vibration sources can be determined with potentially high accuracy, i.e., the exact X, Y, and Z coordinates in 3-D space. Blunt-force impact events caused by different types of implements, for example, a human foot, a water bottle, and various metal objects, are also expected to be identified concurrently by using more complex ML algorithms. For locating multiple impact events that occur simultaneously at different positions in 3-D space, a sensor network combined with more advanced ML algorithms should be employed. However, considering that the fundamental basis of the technique is the spatial anisotropy of matter in physical structures and spaces, the unique signature of an arbitrary blunt-force impact event is a result of the coupling between the blunt-force impact event and the spatial anisotropy of the impacted structure. Once the spatial anisotropy varies, for example, significant cracks in the mechanical transducer (e.g., the optical table and the ground floor in the demonstration), the signatures of the blunt-force impact events may also somewhat vary so that the functionality of the pre-trained system might be comprised.

Nevertheless, the results presented in this paper suggest the promising possibility of combining sensor systems with ML techniques for intelligent sensing applications. The sensor system employed should possess high fidelity, high sensitivity, high resolution, a rapid response time, and a high signal-to-noise ratio for the measurands. The raw data that such sensor systems produce

Optics EXPRESS

is exceedingly rich in information, including expected signals corresponding to variations of the measurands and abnormal "noise" that can be mined for new information not previously identified. Using ML techniques to extract useful meanings from the rich information opens up new avenues for probing mundane events to discover new phenomena.

5. Conclusion

In conclusion, we have demonstrated an intelligent ML-assisted FOI sensor system, resulting in expanded functionality. The ML techniques employed could effectively and efficiently extract the information obtained from a high-resolution 1-D FOI that was useful for detecting blunt-force impact events in the 3-D surrounding space. We predicated this concept on the basis that the base substrate on which the FOI was mounted acted as an anisotropic mechanical coupling transducer, which effectively enabled a single 1-D sensor to sense 3-D space. Different positions in the 3-D surrounding space of the FOI in which blunt-force impact events occurred were successfully identified with excellent accuracy (>99%) using the method of sensing vibrations. It is envisioned that the work presented in this paper may inspire researchers in the fields of sensing and measurement, and open new avenues for developing a new generation of powerful sensors or sensor networks. These sensors, with expanded functionalities and enhanced intelligence, may provide rich information and, in turn, data-driven insights into significant problems. For example, this work suggests that a single 1-D FOI system can monitor the movements of an object, such as a human or a truck, in a clandestine illicit drug zone. Thus, a single-point 1-D sensor system combined with ML can be deployed as a robust and cost-effective spatially distributed sensor system.

Funding

Army Research Laboratory (W911NF-14-2-0034); Leonard Wood Institute (LWI-2018-006).

Acknowledgements

Research was sponsored by the Leonard Wood Institute in cooperation with the U.S. Army Research Laboratory and was accomplished under Cooperative Agreement Number W911NF-142-0034. The views and conclusions contained in this document are those of the authors and should not be interpreted as representing the official policies, either expressed or implied, of the Leonard Wood Institute, the Army Research Laboratory or the U.S. Government. The U.S. Government is authorized to reproduce and distribute reprints for Government purposes notwithstanding any copyright notation hereon.

Disclosures

The authors declare no conflicts of interest.

References

1. E. Udd and W. B. Spillman Jr, *Fiber optic sensors: an introduction for engineers and scientists* (John Wiley & Sons, 2011).
2. H. Guo, G. Xiao, N. Mrad, and J. Yao, "Fiber optic sensors for structural health monitoring of air platforms," Sensors **11**(4), 3687–3705 (2011).
3. A. D. Kersey, "Optical fiber sensors for permanent downwell monitoring applications in the oil and gas industry," IEICE Trans. Electron. **83**(3), 400–404 (2000).
4. P. Roriz, O. Frazão, A. B. Lobo-Ribeiro, J. L. Santos, and J. A. Simões, "Review of fiber-optic pressure sensors for biomedical and biomechanical applications," J. Biomed. Opt. **18**(5), 050903 (2013).
5. R. T. Coates, D. E. Miller, A. H. Hartog, C. A. Wilson, D. Brady, H. Menkiti, F. M. Auzerais, and I. D. R. Bradford, "Detection of seismic signals using fiber optic distributed sensors," U.S. Patent No. 8,605,542 (2013).
6. G. Gagliardi, M. Salza, S. Avino, P. Ferraro, and P. De Natale, "Probing the ultimate limit of fiber-optic strain sensing," Science **330**(6007), 1081–1084 (2010).

Optics EXPRESS

7. J. Ma, W. Jin, H. L. Ho, and J. Y. Dai, "High-sensitivity fiber-tip pressure sensor with graphene diaphragm," Opt. Lett. **37**(13), 2493–2495 (2012).
8. Y. Wang, H. Yuan, X. Liu, Q. Bai, H. Zhang, Y. Gao, and B. Jin, "A Comprehensive Study of Optical Fiber Acoustic Sensing," IEEE Access **7**, 85821–85837 (2019).
9. F. Xu, J. Shi, K. Gong, H. Li, R. Hui, and B. Yu, "Fiber-optic acoustic pressure sensor based on large-area nanolayer silver diaghragm," Opt. Lett. **39**(10), 2838–2840 (2014).
10. J. A. Guggenheim, J. Li, T. J. Allen, R. J. Colchester, S. Noimark, O. Ogunlade, I. P. Parkin, I. Papakonstantinou, A. E. Desjardins, E. Z. Zhang, and P. C. Beard, "Ultrasensitive plano-concave optical microresonators for ultrasound sensing," Nat. Photonics **11**(11), 714–719 (2017).
11. Z. Glasser, Y. Ofer, R. Abramov, D. Gotliv, and S. Sternklar, "High speed and high sensitivity fiber Bragg grating interrogator based on the RF phase-shift technique," Opt. Commun. **428**, 240–244 (2018).
12. M. I. Jordan and T. M. Mitchell, "Machine learning: Trends, perspectives, and prospects," Science **349**(6245), 255–260 (2015).
13. K. J. Bergen, P. A. Johnson, V. Maarten, and G. C. Beroza, "Machine learning for data-driven discovery in solid Earth geoscience," Science **363**(6433), eaau0323 (2019).
14. D. J. Lary, A. H. Alavi, A. H. Gandomi, and A. L. Walker, "Machine learning in geosciences and remote sensing," Geosci. Front. **7**(1), 3–10 (2016).
15. A. E. Maxwell, T. A. Warner, and F. Fang, "Implementation of machine-learning classification in remote sensing: An applied review," Int. J. Remote Sens. **39**(9), 2784–2817 (2018).
16. G. Mountrakis, J. Im, and C. Ogole, "Support vector machines in remote sensing: A review," ISPRS J. Photogramm. **66**(3), 247–259 (2011).
17. Z. Li, M. A. Meier, E. Hauksson, Z. Zhan, and J. Andrews, "Machine learning seismic wave discrimination: Application to earthquake early warning," Geophys. Res. Lett. **45**(10), 4773–4779 (2018).
18. T. Perol, M. Gharbi, and M. Denolle, "Convolutional neural network for earthquake detection and location," Sci. Adv. **4**(2), e1700578 (2018).
19. B. J. Erickson, P. Korfiatis, Z. Akkus, and T. L. Kline, "Machine learning for medical imaging," Radiographics **37**(2), 505–515 (2017).
20. H. Greenspan, B. Van Ginneken, and R. M. Summers, "Guest editorial deep learning in medical imaging: Overview and future promise of an exciting new technique," IEEE Trans. Med. Imaging **35**(5), 1153–1159 (2016).
21. N. Borhani, E. Kakkava, C. Moser, and D. Psaltis, "Learning to see through multimode fibers," Optica **5**(8), 960–966 (2018).
22. P. Wang and J. Di, "Deep learning-based object classification through multimode fiber via a CNN-architecture SpeckleNet," Appl. Opt. **57**(28), 8258–8263 (2018).
23. B. Rahmani, D. Loterie, G. Konstantinou, D. Psaltis, and C. Moser, "Multimode optical fiber transmission with a deep learning network," Light: Sci. Appl. **7**(1), 69 (2018).
24. P. Caramazza, O. Moran, R. Murray-Smith, and D. Faccio, "Transmission of natural scene images through a multimode fibre," Nat. Commun. **10**(1), 2029 (2019).
25. A. R. Cuevas, M. Fontana, L. Rodriguez-Cobo, M. Lomer, and J. M. López-Higuera, "Machine Learning for Turning Optical Fiber Specklegram Sensor into a Spatially-Resolved Sensing System. Proof of Concept," J. Lightwave Technol. **36**(17), 3733–3738 (2018).
26. B. Xu, X. Zhang, J. Jiang, K. Liu, S. Wang, X. Fan, L. Jiang, Y. Li, Y. Chu, and T. Liu, "Method of damage location determination based on a neural network using a single fiber Bragg grating sensor," Appl. Opt. **58**(26), 7251–7257 (2019).
27. X. Geng, S. Lu, M. Jiang, Q. Sui, S. Lv, H. Xiao, Y. Jia, and L. Jia, "Research on FBG-based CFRP structural damage identification using BP neural network," Photonic Sens. **8**(2), 168–175 (2018).
28. S. S. Mahmoud and J. Katsifolis, "Robust event classification for a fiber optic perimeter intrusion detection system using level crossing features and artificial neural networks," Proc. SPIE **7677**, 767708 (2010).
29. Y. Zhuang, Y. Chen, C. Zhu, R. E. Gerald, and J. Huang, "Probing changes in tilt angle with 20 nanoradian resolution using an extrinsic Fabry-Perot interferometer-based optical fiber inclinometer," Opt. Express **26**(3), 2546–2556 (2018).
30. X. Zhou and Q. Yu, "Wide-range displacement sensor based on fiber-optic Fabry–Perot interferometer for subnanometer measurement," IEEE Sens. J. **11**(7), 1602–1606 (2011).
31. I. Daubechies, "The wavelet transform, time-frequency localization and signal analysis," IEEE Trans. Inform. Theory **36**(5), 961–1005 (1990).
32. P. S. Addison, "Wavelet transforms and the ECG: a review," Physiol. Meas. **26**(5), R155–R199 (2005).
33. J. Andén and S. Mallat, "Deep scattering spectrum," IEEE Trans. Signal Process. **62**(16), 4114–4128 (2014).
34. V. Vapnik, *The nature of statistical learning theory* (Springer science & business media, 2013).
35. K. Hacioglu and W. Ward, "Question classification with support vector machines and error correcting codes," Proceedings of HLT-NAACL **2**, 28–30 (2003).
36. E. D. Übeyli, "ECG beats classification using multiclass support vector machines with error correcting output codes," Digit. Signal Process. **17**(3), 675–684 (2007).
37. S. Dreiseitl and L. Ohno-Machado, "Logistic regression and artificial neural network classification models: a methodology review," J. Biomed. Inform. **35**(5-6), 352–359 (2002).

Optics EXPRESS

38. Y. LeCun, Y. Bengio, and G. Hinton, "Deep learning," Nature **521**(7553), 436–444 (2015).
39. I. Goodfellow, Y. Bengio, and A. Courville, *Deep learning* (MIT press, 2016).
40. C. M. Bishop, *Neural networks for pattern recognition* (Oxford university press, 1995).
41. T. P. Vogl, J. Mangis, A. Rigler, W. Zink, and D. Alkon, "Accelerating the convergence of the back-propagation method," Biol. Cybern. **59**(4-5), 257–263 (1988).
42. P. Kim, *Matlab deep learning* (Machine Learning, Neural Networks and Artificial Intelligence 130, 2017).